Radar Coincidence Imaging With a Uniform Circular Array

RUI LI[1], YING LUO [1,2,3], (Member, IEEE), QUN ZHANG [1,2,3], (Senior Member, IEEE), YI-JUN CHEN[4], AND DAN WANG [1,3]

[1]Institute of Information and Navigation, Air Force Engineering University, Xi'an 710077, China
[2]Key Laboratory for Information Science of Electromagnetic Waves, Ministry of Education, Fudan University, Shanghai 200433, China
[3]Collaborative Innovation Center of Information Sensing and Understanding, Xi'an 710077, China
[4]College of Information Engineering, Engineering University of PAP, Xi'an 710086, China

Corresponding author: Ying Luo (luoying2002521@163.com)

ABSTRACT Radar coincidence imaging (RCI), used in conjunction with a uniform circular array (UCA), is presented in this paper. When performing two-dimensional (2-D) imaging for a target, using RCI in conjunction with a uniform linear array (ULA), in three-dimensional (3-D) coordinates, the symmetry phenomenon occurs in certain situation. To overcome this problem, using RCI with a UCA is proposed. First, the symmetry phenomenon of RCI with a ULA and the causes are introduced. Then, the RCI method with a UCA is presented, the signal model is given based on the UCA, and the imaging method is introduced. Finally, the general relationship between the resolution of RCI with a UCA and the independent characteristic of the reference radiation field is analyzed. In view of this, RCI with a UCA has better adaptability to 2-D imaging in 3-D coordinates. Simulation results validate the theoretical analysis and the imaging method.

INDEX TERMS Radar coincidence imaging, spatial autocorrelation, symmetrical images, uniform circular array.

I. INTRODUCTION

As a method for all-weather, all-day and long-range information acquisition, radar imaging has more advantages than optical imaging and has been widely utilized in civilian and military applications [1]–[6]. A synthetic aperture radar (SAR) or an inverse synthetic aperture radar (ISAR) requires the translational or rotational motions of a target in the azimuth positions corresponding to the radar; however, this introduces challenges for motion compensation. Though some methods have been proposed to address this problem [7]–[15], range-Doppler-based imaging methods, such as SAR and ISAR imaging, require long observing time, which causes difficulties when performing fast imaging. Compared with SAR and ISAR imaging, radar coincidence imaging (RCI), originated from optical ghost imaging [16]–[19], is highly effective for rapid real-time imaging, and is suitable static or quasi-stationary targets [20], [21]. The ability of RCI processing to simplify the complicated motion compensation

of a non-cooperative target make it applicable to both cooperative and non-cooperative targets.

In recent years, RCI is proposed and researched extensively [20]–[26]. There is a mode of the correlation between A and B in the RCI processing, where A is the reference radiation field and B is the echo. Importantly, it is essential that A requires the time-space independence. In order to acquire the time-space independent reference radiation field, the core for achieving RCI is to design the transmitted signal. Consequently, in [20], a multi-transmitting configuration with multiple independent sub-sources is reasonable for RCI and is used to produce the time-space independent signals. The time-space independent reference radiation field is calculated with high resolution but no target information. On the contrary, the echoes have no spatial resolution but carry the target information. Therefore, RCI images can be acquired by processing the reference radiation field and the echoes together.

Based on the typical configuration of the RCI system, simulation results show that the resolution is related to several factors [20], [23], [25], [27], such as the transmitted

signals, the array geometry, as well as the reconstruction algorithms. The resolution of coincidence imaging, as derived using the second-order correlation method, is proportional to the wavelength and inversely proportional to the limited size of the source [25]. Based on a uniform one-dimensional (1-D) antenna array and a phase and amplitude modulation signal, the general relationship between the RCI resolution and the deployment of a microwave source was analyzed in [25]. The derivation of the angular-resolution limit of an RCI system is based on a uniform spacing linear array and a frequency random modulation signal [28]. High-resolution RCI requires the reference radiation field to be independent of time and space. This independence depends on the random signal waveform and the array geometry. Furthermore, RCI can be enhanced by exploiting the target prior information in the image reconstruction [29], [30].

As a novel imaging mode, several problems have been investigated for the RCI method, i.e., RCI with different errors [22], [24], resolution analysis of RCI [28], construction of radiation field [26], [31]. However, current research into RCI has focused on two-dimensional (2-D) coordinates, and this means that the target and radar are in the same plane, and the imaging area is only selected in this plane, which limits the application of RCI in three-dimensional (3-D) coordinates. Otherwise, the RCI system most adopts the uniform linear array (ULA), and the research on RCI using other arrays is rare. Hence, this paper examines RCI in 3-D coordinates. However, using RCI with a ULA in 3-D coordinates manifests an interesting phenomenon: when the ULA is not within the plane that the selected imaging area is located in, and the imaging area is symmetrical with respect to the projection line generated by the ULA alignment projecting in this plane, symmetrical images are formed in the imaging area. To avoid this phenomenon, we propose using RCI in conjunction with a uniform circular array (UCA). Moreover, the general relationship between the resolution of RCI with a UCA and the independent characteristic of the reference radiation field is analyzed, and we find that the resolution of RCI with a UCA is also related to the elevation angle.

The rest of this paper is structured as follows. Section II introduces the symmetry phenomenon and its causes. Section III presents RCI with a UCA in 3-D coordinates, introduces the signal model including transmitted signals and received signals, and provides the resolution analysis of RCI with a UCA. Section IV provides our simulation results to demonstrate the validity of the theoretical analysis and the imaging method. In Section V, we draw the conclusions of this paper.

II. SYMMETRY PHENOMENON

At present, the imaging area is selected in the 2-D plane formed by radar and target in most of the researches [20]–[26], and a ULA is used to form spatial independent reference radiation field which can meet the imaging requirements. However, in 3-D coordinates, the selection of imaging area is more flexible. In some cases, it is no longer in the

2-D plane formed by radar and target. In this case, the reference radiation field formed by the ULA no longer satisfies the spatial independence under specific circumstances, and the imaging results will be symmetrical.

When performing 2-D imaging for a target in 3-D coordinates, the symmetry phenomenon occurs in the aforementioned situation using RCI with a ULA. Assume that the ULA is aligned along the X-axis, N elements are distributed in $[b, Nb]$ with equal interval b, the receiving antenna is located at the origin, and a burst of RPM signal consists of D sub-pulses of duration T_p. Then the signal transmitted by the nth element can be expressed as

$$s_n(t, d) = rect\left(\frac{t - d \cdot T_{sub}}{T_p}\right)$$
$$\cdot \exp\left\{j2\pi f_d(t - d \cdot T_{sub}) + j\varphi_n^d\right\} \quad (1)$$

where $rect(t/T_p)$ is a rectangular window function that serves to constrain the imaging time and to ensure that the signals transmitted by the radar elements are effectively captured at the imaging cells [25]. $f_d = f_c + d \cdot \Delta f$, $d = 0, 1, \cdots, D - 1$ is the frequency of the dth sub-pulse, f_c is the carrier frequency, T_{sub} and Δf denote the sub-pulse repetition interval and the frequency increment, respectively, and $\{\varphi_n^d, d = 0, 1, \cdots, D - 1\}, n = 1, 2, \cdots, N$ are a set of random sequences uniformly distributed in $[0, 2\pi]$. The random sequences $\{\varphi_n^d, d = 0, 1, \cdots, D - 1\}, n = 1, 2, \cdots, N$ are mutually independent. The cross-correlations of the transmitted signals between the different elements can be computed as

$$R_{nm}(k) = E\left[s_n(t) s_m^*(t - kT_{sub})\right]$$
$$= \sum_{d=k}^{D-1} E\left[s_n(t, d) s_m^*(t - kT_{sub}, d - k)\right]$$
$$= \sum_{d=k}^{D-1} \exp\{j2\pi f_d kT_{sub}\} E\left[\exp\left\{j\left(\varphi_n^d - \varphi_m^{d-k}\right)\right\}\right]$$
$$= \sum_{d=k}^{D-1} \exp\{j2\pi f_d kT_{sub}\} R_{\varphi_n\varphi_m}(k) \quad \begin{pmatrix} 0 \le k \le D - 1 \\ k \in \mathbb{Z} \end{pmatrix}$$
$$(2)$$

where $E[*]$ denotes the expected value, $R_{\varphi_n\varphi_m}(k) = E\left[\exp\left\{j\left(\varphi_n^d - \varphi_m^{d-k}\right)\right\}\right]/E\left[\exp\left\{j\left(\varphi_n^d - \varphi_m^d\right)\right\}\right]$ denotes the normalization cross-correlation between $\{\exp\{j\varphi_n^d\}, d = 0, 1, \cdots, D-1\}$ and $\{\exp\{j\varphi_m^d\}, d = 0, 1, \cdots, D - 1\}$. When $n = m$, $R_{\varphi_n\varphi_n}(k)$ denotes the normalization autocorrelation of $\{\exp\{j\varphi_n^d\}, d = 0, 1, \cdots, D - 1\}$. $R_{\varphi_n\varphi_n}(k)$ has the maximum $R_{\varphi_n\varphi_n}(0) = 1$, and $R_{\varphi_n\varphi_n}(k) = 0$ at $k \ne 0$. When $n \ne m$, $R_{\varphi_n\varphi_m}(k) = 0$. Therefore,

$$R_{\varphi_n\varphi_m}(k) = \begin{cases} \delta(k) & (n = m) \\ 0 & (n \ne m), \end{cases}$$

where $\delta(\alpha)$ is an impulse sequence. If $\alpha = 0$, then $\delta(\alpha) = 1$; otherwise $\delta(\alpha) = 0$. Under this condition, the cross-correlation obeys $R_{nm}(k) = D\delta(k)\delta(n - m)$.
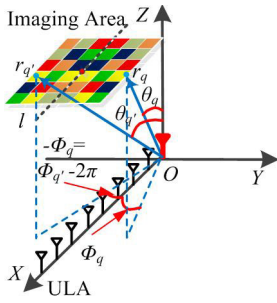
FIGURE 1. The symmetry phenomenon in RCI with a ULA.

As shown in Fig. 1, the imaging area is selected and parallel to the *XOY* plane, and the projection line generated by the ULA alignment is the dotted line *l*. To realize RCI, the imaging area is first discretized as a grid of Q cells. The position vectors of the cells are expressed as $V = \{r_q | q = 1, 2, \cdots, Q\}$, where $r_q = (r_q, \theta_q, \phi_q)^T$ is the position vector of the qth cell. Then, perform the discretization of the time domain in accordance with the time series $t_s = [t_1, t_2, \cdots, t_P]$. According to [25], the measurement matrix element $S_L(t_p, r_q)$ of RCI with a ULA can be expressed as

$$S_L(t_p, r_q) = \sum_{n=1}^{N} \exp\left\{t_p - jk_p\left(2r_q - nb\sin\theta_q\cos\phi_q\right) + j\varphi_n^p\right\}$$
(3)

where t_p denotes the pth sample time, $k_p = 2\pi f_p/c$ denotes the wave number and f_p is the frequency of the sub-pulse. When the imaging area is symmetrical with respect to l, then, for $\forall r_q = (r_q, \theta_q, \phi_q)^T$, $\exists r_{q'} = (r_{q'}, \theta_{q'}, \phi_{q'})^T$, make $r_q = r_{q'}$, $\theta_q = \theta_{q'}$, and $\phi_q + \phi_{q'} = 2\pi$ workable. Hence, $S_L(t_p, r_q) = S_L(t_p, r_{q'})$ can be derived, and the reference radiation field is symmetrical with respect to the dotted line l. In other words, the spatial independence of the reference radiation field is no longer satisfied. It causes that half of column vectors in the measurement matrix repeat the other half, so that r_q and $S_L(t_p, r_q)$ no longer meet the one-to-one correspondence. In this case, the scatterer cannot be correctly reconstructed in the image reconstruction process, i.e., the position of the scatterer cannot be determined.

III. RCI WITH A UCA
A. SIGNAL MODEL
In the RCI system shown in Fig. 2, a UCA antenna consisting of N elements is used as the transmitting antenna. The N elements are assumed to be distributed uniformly around the circle of radius a. Their azimuthal positions are denoted ϕ_n. The receiving antenna is located at the origin. RPM signals are used to ensure that the transmitted signals are temporally and spatially independent, and the parameters of transmitted signals are consistent with those of RCI with a ULA. For a detection point A(r, θ, ϕ), the detection signal can be denoted

$$S_I(t, r) = \sum_{n=1}^{N}\sum_{d=0}^{D-1} s_n(t - \tau_n(r), d)$$
(4)

where $\tau_n(r) = \|r - R_n\|/c$ is the time delay from the nth element to the detection point A, $r = (r, \theta, \phi)^T$ denotes the initial position vector for the detection point A in spherical coordinates, $R_n = (a, \pi/2, 2\pi(n-1)/N)^T$ denotes the position vector of the nth element, and c is the speed of light in a vacuum.

A target is composed of M scatterers. The receiving antenna captures the echo scattered from the target, which can be described by

$$y(t) = \sum_{m=1}^{M} \sigma_m \cdot S_I\left(t - \|r_m - R_r\|/c, r_m\right)$$

$$= \sum_{m=1}^{M} \sigma_m \cdot \left(\sum_{n=1}^{N}\sum_{d=0}^{D-1} s_n\left(t - \tau_n^t(r_m), d\right)\right)$$
(5)

where σ_m and $r_m = (r_m, \theta_m, \phi_m)^T$, respectively, denote the scattering coefficient and the initial position vector of the mth scatterer. $R_r = (0, 0, 0)^T$ denotes the position vector of the receiving antenna, and $\tau_n^t(r_m) = (\|r_m - R_n\| + \|r_m - R_r\|)/c$ denotes the total time delay. Generally, $\|r_m\| \gg \|R_n\|$ and $\|r_m\| \gg \|R_r\|$ in the observation time, hence $\tau_n^t(r_m)$ can be approximated as

$$\tau_n^t(r_m) \approx \left(2r_m - a\sin\theta_m\cos(\phi_m - \phi_n)\right)/c$$
(6)

After the discretization of the time domain in accordance with the time series $t_s = [t_1, t_2, \cdots, t_P]$, the echo vector can be obtained and expressed as $y = [y_1, y_2, \cdots, y_P]^T \in \mathbb{C}^{P\times 1}$, where t_p denotes the pth sample time, and P is the sample number. Hence, y_p can be further expressed as

$$y_p = \sum_{m=1}^{M} \sigma_m \cdot \left(\sum_{n=1}^{N} \exp\left\{t_p - j2\pi f_p \cdot \tau_n^t(r_m) + j\varphi_n^p\right\}\right)$$
(7)

B. IMAGING METHOD
Assuming that the target is located in an imaging area I shown in Fig. 2, and the variation in the phase distribution caused by the motions is ignored, the echo can be expressed as the
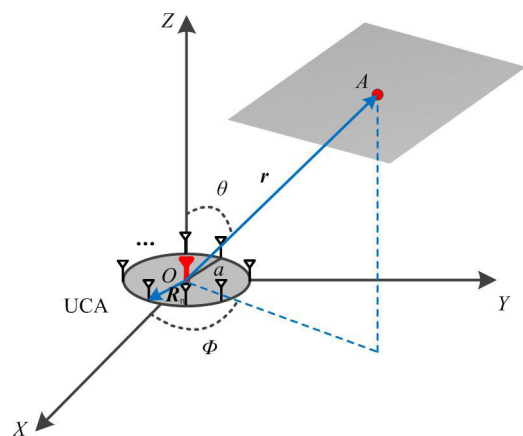

FIGURE 2. RCI system model with a UCA.

superposition of detection signals $S_I(t, r)$ [20]

$$y(t) = \int_I \sigma_r \cdot S_I(t - \|r - R_r\|/c, r) \, dr \tag{8}$$

where σ_r is the scattering coefficient of a scatterer located at r. If there is no scatterer at r, then $\sigma_r = 0$. According to RCI theory, $S_I(t - \|r - R_r\|/c, r)$ is defined as the reference radiation field, which is simply the transform of the detection signal $S_I(t, r)$ with an additional time delay induced by the propagation to the receiving antenna [20]. Hence, the reference radiation field $S(t, r)$ can be expressed as

$$S(t, r) = S_I(t - \|r - R_r\|/c, r)$$
$$\approx \sum_{n=1}^{N} \sum_{d=0}^{D-1} s_n(t - \tau_n^t(r), d)$$
$$= \sum_{n=1}^{N} \sum_{d=0}^{D-1} s_n(t, d) \cdot \exp\{-j2\pi f_d \tau_n^t(r)\} \tag{9}$$

where $\tau_n^t(r)$ denotes the total time delay from the nth element to the receiving antenna, and it can be expressed as

$$\tau_n^t(r) = (\|r - R_n\| + \|r - R_r\|)/c$$
$$\approx (2r - a \sin\theta \cos(\phi - \phi_n))/c \tag{10}$$

To realize RCI, the imaging area is first discretized as a grid of Q cells. The position vectors of the cells are expressed as $V = \{r_q | q = 1, 2, \cdots, Q\}$, where $r_q = (r_q, \theta_q, \phi_q)^T$ is the position vector of the qth cell. The scattering coefficients of these cells form a vector $\sigma = [\sigma_1, \sigma_2, \cdots, \sigma_Q]^T \in \mathbb{C}^{Q \times 1}$. Then, after sampling in accordance with the time series $t_s = [t_1, t_2, \cdots, t_P]$, a reference radiation field vector of the imaging area can be calculated:

$$S_p = [S(t_p, r_1), S(t_p, r_2), \cdots, S(t_p, r_Q)] \tag{11}$$

where

$$S(t_p, r_q) = \sum_{n=1}^{N} \exp\{t_p - jk_p(2r_q - a \sin\theta_q \cos(\phi_q - \phi_n))$$
$$+ j\varphi_n^p\} \tag{12}$$

To make the reference radiation field be independent of time, $P \leq D$, and $\{\varphi_n^p, p = 1, 2, \cdots, P\} \subseteq \{\varphi_n^d, d = 0, 1, \cdots, D - 1\}$, which implies that $\{\varphi_n^p, p = 1, 2, \cdots, P\}$ ia also a random sequence. Hence, the measurement matrix formed by the vectors of reference radiation field can be written as

$$S = [S_1, S_2, \cdots, S_P]^T$$
$$= \begin{bmatrix} S(t_1, r_1) & S(t_1, r_2) & \cdots & S(t_1, r_Q) \\ S(t_2, r_1) & S(t_2, r_2) & \cdots & S(t_2, r_Q) \\ \vdots & \vdots & \ddots & \vdots \\ S(t_P, r_1) & S(t_P, r_2) & \cdots & S(t_P, r_Q) \end{bmatrix} \tag{13}$$

Finally, we consider the influences of noise. The linear imaging model, based on the parameterized method, is expressed as [31]

$$y = S \cdot \sigma + e \tag{14}$$

where $e \in \mathbb{C}^{P \times 1}$ is a noise vector. When the target scatterers are sparse in the imaging area, the above model amounts to a typical compressed sensing (CS) problem. The super-resolution image can be obtained by solving (14). Also, the temporal and spatial independence inherent in the measurement matrix S can affect the imaging performance. Considering the prior information of the noise, we used the sparse Bayesian learning (SBL) algorithm [32] to reconstruct the image. To ensure to reconstruct the image accurately, the sample number requires to satisfy the expression $P \geq K \log_2(Q/K)$, where K denotes the sparse degree of σ [33]. Based on the parameterized method and the SBL algorithm, the imaging process works as follows:

1) Take the sample of the echoes and obtain the echo vector;

2) According to the prior information such as the target position and rough target size, determine the reference point and imaging area, and discretize the imaging area as a grid;

3) Calculate the reference radiation field in the imaging area and obtain the measurement matrix;

4) Solve the linear imaging model and reconstruct the target image.

C. RESOLUTION ANALYSIS
In fact, the RCI resolution is determined by several factors, such as the transmitted signals, the array geometry, as well as the reconstruction algorithms. As the linear imaging model, presented in (14), is generally established with the parameterized method, it is difficult to obtain an analytical expression of the resolution limit theoretically [31]. Still, to give a quantitative analysis of the resolution of RCI with a UCA, the spatial autocorrelation is used to address the spatial resolution. Because of $\Delta f \ll f_c$, the spatial autocorrelation of RCI with a UCA can be expressed as [34]

$$R_S^{space}(r_1, r_2)$$
$$= E[S(t, r_1) S^*(t, r_2)]$$
$$= \sum_{m=1}^{N} \sum_{n=1}^{N} E[s_n(t - \tau_n^t(r_1), p) s_m^*(t - \tau_m^t(r_2), p)]$$
$$= \sum_{m=1}^{N} \sum_{n=1}^{N} \frac{\exp\{j2\pi f_p(\tau_m^t(r_2) - \tau_n^t(r_1))\}}{E[\exp\{j(\varphi_n^p - \varphi_m^p)\}]}$$
$$\approx \sum_{n=1}^{N} \exp\{j2\pi f_c(\tau_n^t(r_2) - \tau_n^t(r_1))\} \tag{15}$$

where $k_c = 2\pi f_c/c$.

When there are sufficiently many UCA elements and the space deviation is small, the range, elevation, and azimuthal autocorrelations are derived from (15) based on the first order approximation of Taylor expansion and described as follows:

1) When $r_2 - r_1 = (\Delta r, 0, 0)^T$, $R_S^{space}(r_1, r_2)$ can be rewritten as

$$R_S^{space}(\Delta r) \approx \sum_{n=1}^{N} \exp\{j2k_c\Delta r\} = N \exp\{j2k_c\Delta r\} \tag{16}$$

2) When $\boldsymbol{r}_2 - \boldsymbol{r}_1 = (0, \Delta\theta, 0)^T$, $R_S^{space}(\boldsymbol{r}_1, \boldsymbol{r}_2)$ can be rewritten as

$$
\begin{aligned}
R_S^{space}(\Delta\theta) &= \sum_{n=1}^{N} \exp\{-jk_c a \left[\sin(\theta + \Delta\theta) - \sin\theta\right] \\
&\qquad\qquad \cdot \cos(\phi - \phi_n)\} \\
&\approx \sum_{n=1}^{N} \exp\{-jk_c a \cos\theta \cdot \Delta\theta \cos(\phi - \phi_n)\} \\
&\approx \frac{N}{2\pi} \int_0^{2\pi} \exp\{-jk_c a \cos\theta \cdot \Delta\theta \cos(\phi - \varphi)\} \, d\varphi \\
&\approx -N J_0 (k_c a \cos\theta \cdot \Delta\theta)
\end{aligned}
\tag{17}
$$

3) When $\boldsymbol{r}_2 - \boldsymbol{r}_1 = (0, 0, \Delta\phi)^T$, $R_S^{space}(\boldsymbol{r}_1, \boldsymbol{r}_2)$ can be rewritten as

$$
\begin{aligned}
R_S^{space}(\Delta\phi) &= \sum_{n=1}^{N} \exp\{-jk_c a \sin\theta \\
&\qquad \cdot \left[\cos(\phi + \Delta\phi - \phi_n) - \cos(\phi - \phi_n)\right]\} \\
&\approx \sum_{n=1}^{N} \exp\{jk_c a \sin\theta \cdot \Delta\phi \sin(\phi - \phi_n)\} \\
&\approx \frac{N}{2\pi} \int_0^{2\pi} \exp\{-jk_c a \sin\theta \cdot \Delta\phi \\
&\qquad\qquad \cdot \cos(\pi/2 + \phi - \varphi)\} \, d\varphi \\
&\approx -N J_0 (k_c a \sin\theta \cdot \Delta\phi)
\end{aligned}
\tag{18}
$$

where $J_0(*)$ denotes the zeroth-order Bessel function of the first kind. (16) implies that the range resolution is poor. In other words, the utilization of the UCA cannot achieve range resolution. However, the wideband signals can be exploited to distinguish the distance information from the time dimension [31]. The relationship between signal bandwidth and resolution can be measured by calculating the temporal autocorrelation, and the temporal autocorrelation can be expressed as

$$
\begin{aligned}
&R_S^{time}(\tau) \\
&= E\left[S(t, r) S^*(t - \tau, r + \Delta r) \right] \\
&= E\left[\left(\sum_{n=1}^{N} \sum_{d=0}^{D-1} s_n(t, d) \right) \cdot \left(\sum_{m=1}^{N} \sum_{d=0}^{D-1} s_m^*(t - \tau, d) \right) \right] \\
&= \sum_{m=1}^{N} \sum_{n=1}^{N} \sum_{d=0}^{D-1} E\left[s_n(t, d) s_m^*(t - \tau, d) \right] \\
&= \sum_{m=1}^{N} \sum_{n=1}^{N} \sum_{d=0}^{D-1} \exp\{j2\pi f_d \tau\} \cdot E\left[\exp\left\{ j\left(\varphi_n^d - \varphi_m^d \right) \right\} \right] \\
&= \sum_{m=1}^{N} \sum_{n=1}^{N} \sum_{d=0}^{D-1} \exp\{j2\pi f_d \tau\} \cdot R_{\varphi_n \varphi_m}(0) \\
&= N \sum_{d=0}^{D-1} \exp\{j2\pi f_d \tau\}
\end{aligned}
\tag{19}
$$

The main lobe's 3 dB width of $\left| R_S^{time}(\tau) \right| / \left| R_S^{time}(0) \right|$ can be used to express the resolution, and $\left| R_S^{time}(\tau) \right| / \left| R_S^{time}(0) \right|$ can

be expressed as

$$
\begin{aligned}
\frac{\left| R_S^{time}(\tau) \right|}{\left| R_S^{time}(0) \right|} &\approx \left| \frac{1 - \exp\{j2\pi D \Delta f \tau\}}{1 - \exp\{j2\pi \Delta f \tau\}} \right| \\
&= \left| \frac{\sin(\pi D \Delta f \tau)}{\pi D \Delta f \tau} \right| \\
&= \left| \frac{\sin(2\pi D \Delta f \Delta r / c)}{2\pi D \Delta f \Delta r / c} \right|
\end{aligned}
\tag{20}
$$

Hence, according to (20), the range resolution can be derived

$$
\rho_r \propto \frac{1}{D \Delta f} = \frac{1}{B}
\tag{21}
$$

(17) and (18) imply that the elevation and azimuthal resolutions can be obtained because of the existence of the main lobe. The main lobe's 3 dB width of $\left| R_S^{space}(*) \right| / \left| R_S^{space}(0) \right|$, where "$*$" respectively refer to $\Delta\theta$ and $\Delta\phi$, can be used to express the resolution. Hence, according to the property of the Bessel function, the elevation and azimuthal resolutions are respectively derived

$$
\rho_\theta \propto \frac{1}{k_c a \cos\theta} \qquad \rho_\phi \propto \frac{1}{k_c a \sin\theta}
\tag{22}
$$

From (21) and (22), the range resolution is inversely proportional to the signal bandwidth; the elevation and azimuthal resolutions are both proportional to the wavelength and inversely proportional to the size of the UCA. This conclusion is in accordance with the previous research results [25]. Besides, when $\theta \in (0, \pi/2)$, the elevation resolution is proportional to the elevation angle θ, while the azimuthal resolution is inversely proportional to the elevation angle θ, i.e., the elevation resolution ability become better with the elevation angle θ decreasing and the azimuthal resolution ability become better with the elevation angle θ increasing.

IV. SIMULATION AND ANALYSIS
This study performs simulation experiments to validate the proposed analysis and imaging method. A 16-transmitter 1-receiver UCA with radius $a = 1\,m$ and a 16-transmitter 1-receiver ULA aligned along the X-axis with interval $b = 1\,m$ are used. Every element transmits the RPM signal with carrier frequency $f_c = 9.5\,GHz$, bandwidth $B = 500\,MHz$, and pulse duration $T_p = 2\,\mu s$. Also, the RPM signal phase is randomly distributed $[0, 2\pi]$. The white complex Gaussian noises are added, whose signal-to-noise ratio is $SNB = 10\,dB$.

A. SYMMETRY PHENOMENON
Two different kinds of imaging areas and targets are chosen to validate the symmetry phenomenon.

If the reference point of the imaging area is chosen to be $(100\,m, \pi/6\,rad, 0\,rad)^T$ and the imaging area is set as $0.4\,rad \times 0.4\,rad$, it satisfies the condition of symmetry phenomenon. The imaging area is discretized to a grid of 21×21 cells with an elevation resolution of $\rho_\theta = 0.02\,rad$ and an azimuth resolution of $\rho_\phi = 0.02\,rad$. Suppose that there are 3 scatterers on a target. The reflection coefficients of the 3 scatterers are all one. The scatterers are located at
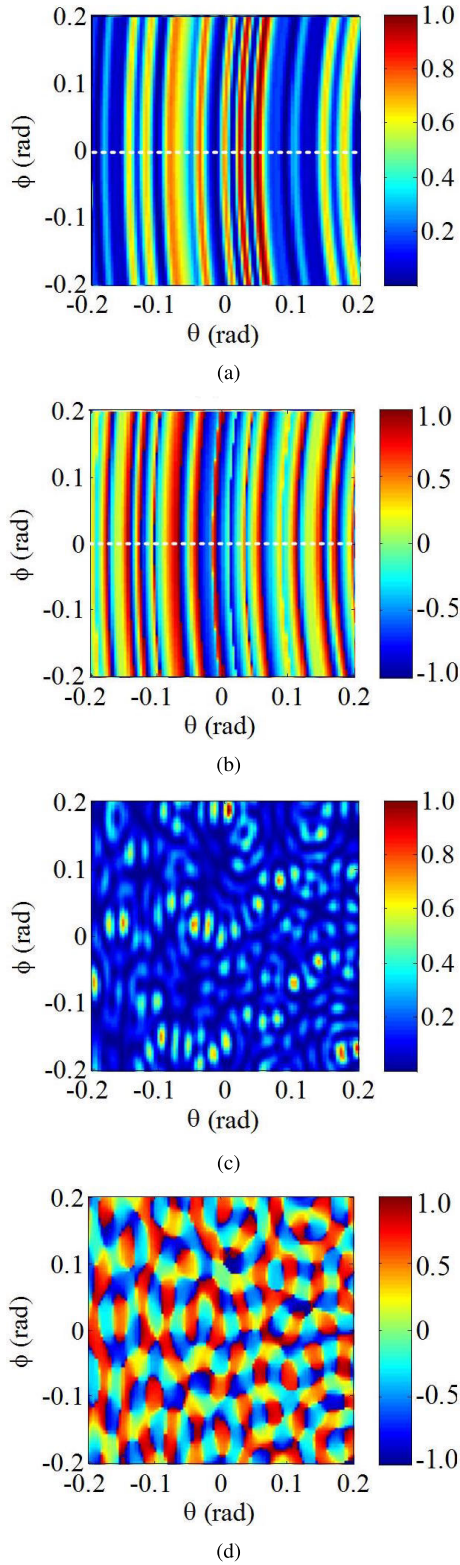
(a)

(b)

(c)

(d)

FIGURE 3. With the imaging area of 0.4 *rad* × 0.4 *rad* at (100 *m*, $\pi/6$ *rad*, 0 *rad*)^T discretized to a grid of 101 × 101, radiation distribution of reference radiation field formed by different arrays.

the cell centers. Hence, the unknown scattering coefficient vector of the imaging area σ is K-sparse, and $K = 3$. The sample number is chosen to be $P = 255$, which satisfies

the expression $P \geq K \log_2 (Q/K)$. With the aforementioned imaging process implemented, the symmetry phenomenon of RCI with a ULA is displayed.

As shown in Fig. 3, intensity distribution and phase-front distribution of reference radiation field formed by ULA are depicted in Fig. 3(a) and (b), and intensity distribution and phase-front distribution of reference radiation field formed by UCA are depicted in Fig. 3(c) and (d). In view of Fig. 3(a) and (b), the reference radiation field formed by the ULA is symmetrical with respect to the white dotted line. However, the reference radiation field formed by the UCA is spatially independent, as depicted in Fig. 3(c) and (d). Therefore, RCI with a ULA yields the symmetrical images shown in Fig. 4(a). Two target images were reconstructed,
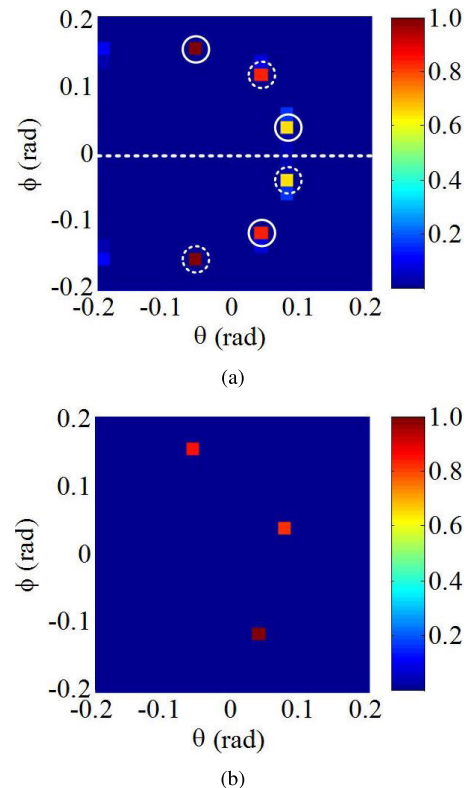

(a)

(b)

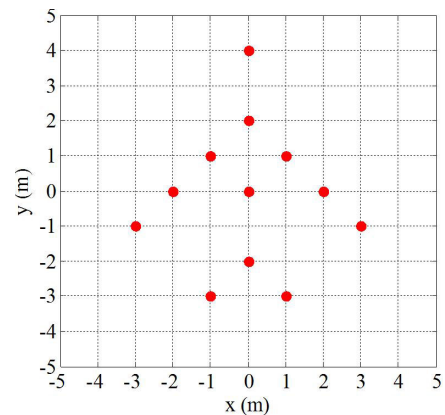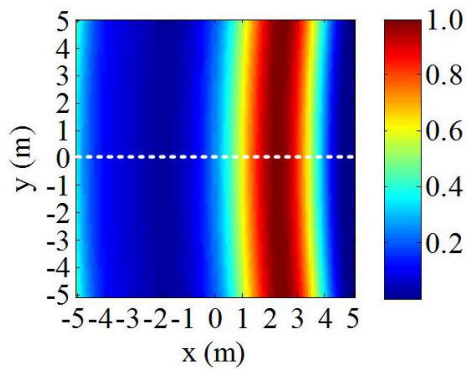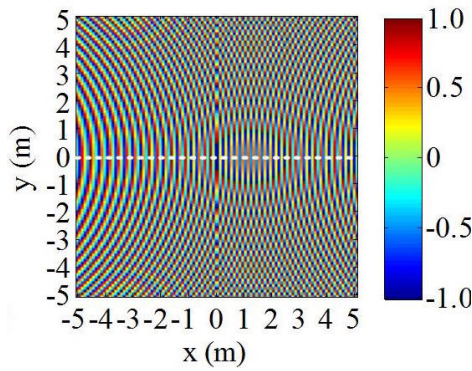**FIGURE 4.** Imaging results using RCI with different transmitting arrays at the reference point (100 *m*, $\pi/6$ *rad*, 0 *rad*)^T.
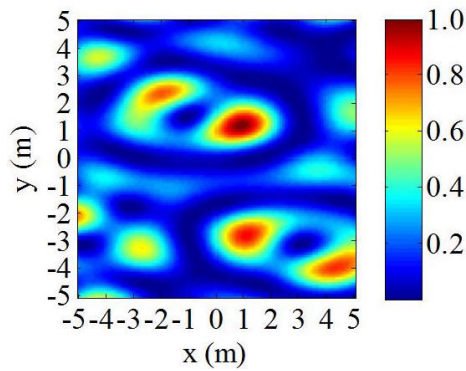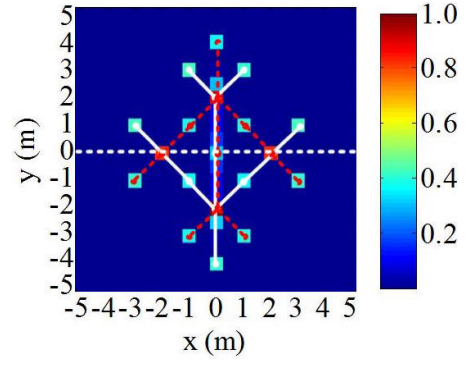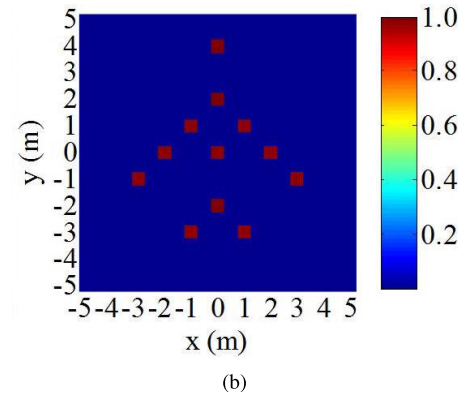

FIGURE 5. Airplane arget model.

(a)

(b)

(c)
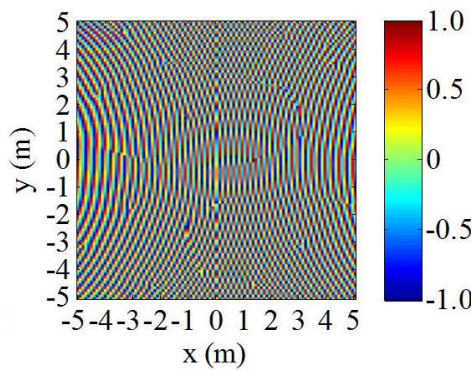
(d)

FIGURE 6. With the imaging area of $10\,m \times 10\,m$ at $(100\,m, \pi/4\,rad, 0\,rad)^T$ discretized to a grid of 101×101, radiation distribution of reference radiation field formed by different arrays.

(a)

(b)

FIGURE 7. Imaging results using RCI with different transmitting arrays at the reference point $(100\,m, \pi/4\,rad, 0\,rad)^T$.

represented by white solid circles and white dotted circles, which are symmetrical with respect to the white dotted lines. By comparison, using RCI with a UCA can correctly reconstruct the target image shown in Fig. 4(b).

Also, the reference point of the imaging area is chosen to be $(100\,m, \pi/4\,rad, 0\,rad)^T$. A plane of $10\,m \times 10\,m$ is set as the imaging area. As depicted in Fig. 5, an airplane target model with 12 scatterers is used as a simulation model. The reflection coefficients of 12 scatterers are all one. The scatterers are located at the cell centers. Hence, the unknown scattering coefficient vector of the imaging area σ is K-sparse, and $K = 12$. The sample number is chosen to be $P = 255$, which satisfies the expression $P \geq K \log_2 (Q/K)$.

With the aforementioned imaging process implemented, the symmetry phenomenon of RCI with a ULA is displayed. As depicted in Fig. 6(a) and (b), the reference radiation field formed by the ULA is symmetrical with respect to the white dotted line. However, the reference radiation field formed by the UCA is spatially independent, as depicted in Fig. 6(c) and (d). Therefore, RCI with a ULA yields the symmetrical images shown in Fig. 7(a). Two target images were reconstructed, represented by white solid lines and red dotted lines, which are symmetrical with respect to the white dotted lines. By comparison, using RCI with a UCA can correctly reconstruct the target image shown in Fig. 7(b).
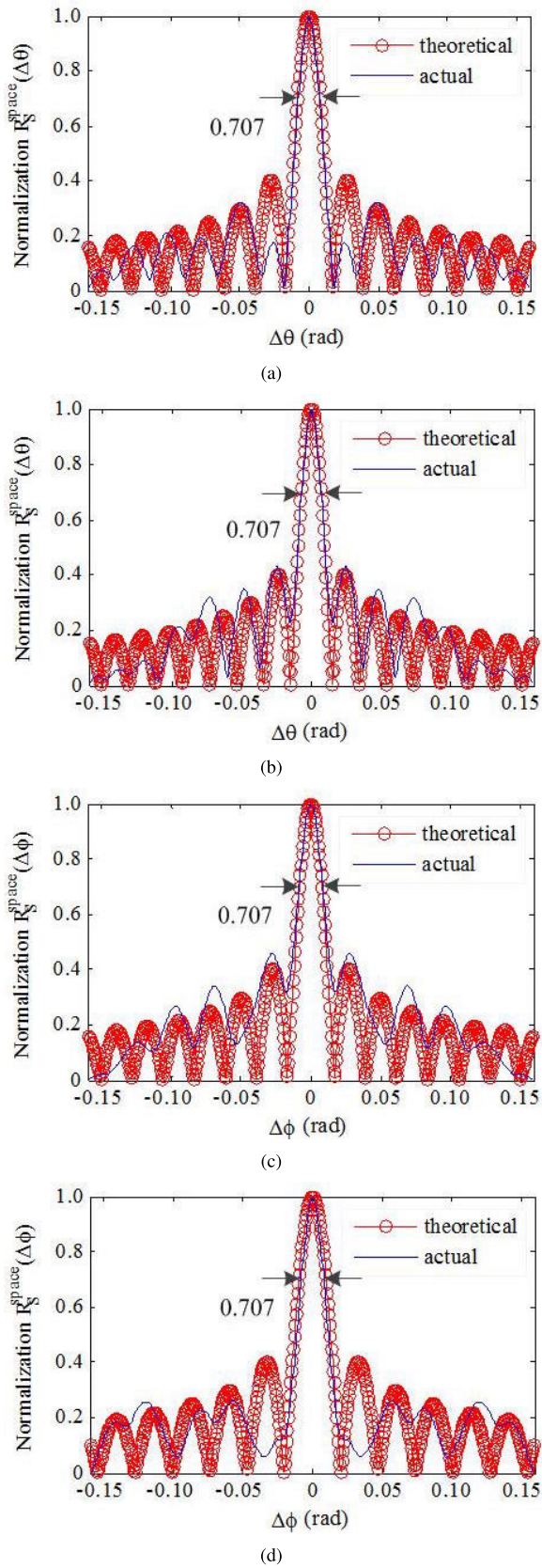
FIGURE 8. Theoretical and actual autocorrelations of the reference radiation field.
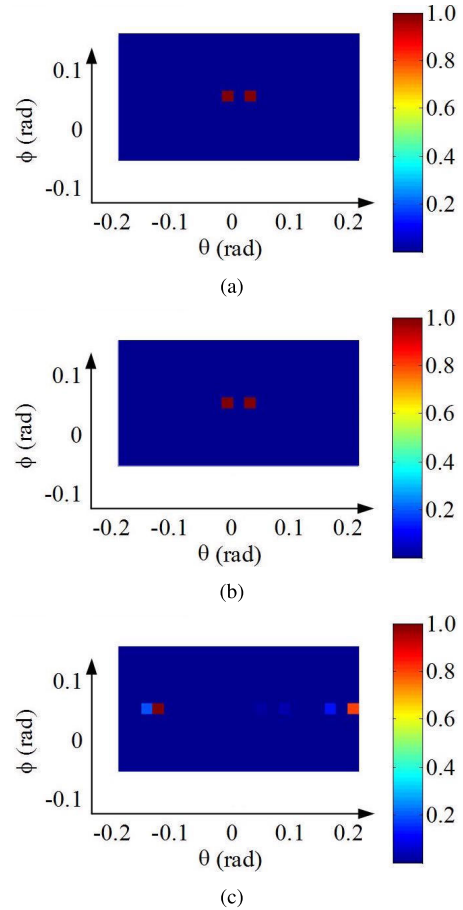

FIGURE 9. For the two point-targets being 0.04 *rad* apart in elevation direction, imaging results at different elevation directions.

B. RESOLUTION OF RCI WITH A UCA

The derivations of (17) and (18) are validated in this section firstly. At the reference point $(100\,m,\ \pi/4\,rad,\ \pi/10\,rad)^T$ and $(100\,m,\ \pi/5\,rad,\ \pi/10\,rad)^T$, the theoretical and actual normalization autocorrelations of the reference radiation field in the elevation and azimuth directions are shown in Fig. 8, where curves express the normalization auto-correlation modulus. Fig. 8 (a) and (b) show that the theoretical and actual normalization autocorrelations of the reference radiation field in the elevation direction at the reference point $(100\,m,\ \pi/4\,rad,\ \pi/10\,rad)^T$ and $(100\,m,\ \pi/5\,rad,\ \pi/10\,rad)^T$, respectively. Fig. 8 (c) and (d) show that the theoretical and actual normalization autocorre-lations of the reference radiation field in the azimuth direc-tion at the reference point $(100\,m,\ \pi/4\,rad,\ \pi/10\,rad)^T$ and $(100\,m,\ \pi/5\,rad,\ \pi/10\,rad)^T$, respectively.

In the elevation and azimuthal directions, the main lobe-like sections of the theoretical autocorrelations are almost identical with those of the actual autocorrelations, though there are some errors in other regions. This implies that the derived results can effectively express the elevation and azimuthal autocorrelations. Hence, the expressions of the
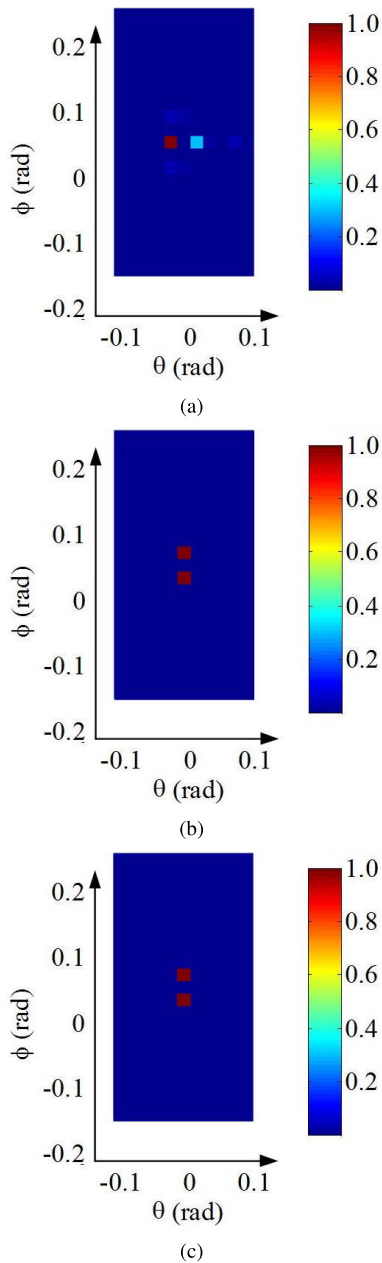
(a)

(b)

(c)

FIGURE 10. For the two point-targets being 0.04 *rad* apart in azimuthal direction, imaging results using RCI with a UCA at different elevation directions.

elevation and azimuthal resolutions can be derived correctly. As shown in Fig. 8, the resolution is proportional to the 3dB width of the main lobe, as indicated by the arrows.

Because the aforementioned elevation and azimuthal resolutions are not analytical expressions of the resolution limit theoretically, they only indicate the general proportional relationship between the resolution and the array geometry of the UCA. Therefore, by implementing imaging for the two point-targets being 0.04 *rad* apart at different elevation directions, imaging performance is used to indirectly reflect the resolution. The mean square error (MSE) is used as a metric for quantifying imaging performance.

When the two point-targets are 0.04 *rad* apart in elevation direction, imaging results at different elevation directions are shown in Fig. 9 and the MSEs of images at different elevation directions are listed in Table 1. With the elevation angle θ increasing, the MSE gradually increases. It implies that the imaging performance becomes worse and worse, so that the two point-targets are no longer reconstructed correctly at $\theta = \pi/3\,rad$. So, it indirectly reflects that the elevation resolution becomes worse.

TABLE 1. MSEs of images at different elevation directions.

θ	$\pi/6\,rad$	$\pi/4\,rad$	$\pi/3\,rad$
MSE	$-20.32dB$	$-19.94dB$	$0.31dB$

By contrary, when the two point-targets are 0.04 *rad* apart in azimuthal direction, imaging results at different elevation directions are shown in Fig. 10 and the MSEs of images at different elevation directions are listed in Table 2. With the elevation angle θ increasing, the MSE gradually decreases. It implies that the imaging performance becomes better and better, though the two point-targets are not reconstructed correctly at $\theta = \pi/6\,rad$. So, it indirectly reflects that the azimuthal resolution becomes better.

TABLE 2. MSEs of images at different elevation directions.

θ	$\pi/6\,rad$	$\pi/4\,rad$	$\pi/3\,rad$
MSE	$0.41dB$	$-18.73dB$	$-19.16dB$

From the above simulations, it can be found that the symmetry phenomenon and the resolution analyses have been validated.

V. CONCLUSION

When using RCI in conjunction with a ULA in 3-D coordinates, the symmetry phenomenon occurs in certain situation. It is first proposed and the causes are introduced. To avoid this phenomenon, hence, this study proposes using RCI in conjunction with a UCA. Because the reference radiation field formed by the UCA is independent, the symmetry phenomenon does not occur. This suggests that the method can obtain the accurate imaging result without symmetrical images. Therefore, in 3-D coordinates, using RCI with a UCA is not limited by the target location, it can image for the target in any plane, and its adaptability is stronger.

Besides, the general relationship between the resolution of RCI with a UCA and the independent characteristic of the reference radiation field is analyzed. It has been found that the resolution is not only related to the signal wavelength and the size of the UCA, but also to the elevation angle. The elevation resolution and the azimuth resolution are mutually restricted. With the increase of elevation angle, the former becomes lower and lower, while the latter becomes higher and higher. This indicates that the resolution of RCI with a UCA is sensitive to the choice of reference point in the imaging area. How to choose the appropriate elevation angle to maximize

the two resolutions is worth investigating. Therefore, we will further study in the future.

REFERENCES

[1] Y.-J. Chen, Q. Zhang, Y. Luo, and K.-M. Li, "Multi-target radar imaging based on phased-MIMO technique—Part I: Imaging algorithm," *IEEE Sensors J.*, vol. 17, no. 19, pp. 6185–6197, Oct. 2017.

[2] X. Ye, F. Zhang, Y. Yang, D. Zhu, and S. Pan, "Photonics-based high-resolution 3D inverse synthetic aperture radar imaging," *IEEE Access*, vol. 7, pp. 79503–79509, 2019.

[3] Y. Zhou, L. Zhang, C. Xing, P. Xie, and Y. Cao, "Target three-dimensional reconstruction from the multi-view radar image sequence," *IEEE Access*, vol. 7, pp. 36722–36735, 2019.

[4] R. Iglesias, A. Aguasca, X. Fabregas, J. J. Mallorqui, D. Monells, C. López-Martínez, and L. Pipia, "Ground-based polarimetric SAR interferometry for the monitoring of terrain displacement phenomena—Part II: Applications," *IEEE J. Sel. Topics Appl. Earth Observ. Remote Sens.*, vol. 8, no. 3, pp. 994–1007, Mar. 2014.

[5] X. R. Bai and Z. Bao, "High-resolution 3D imaging of precession cone-shaped targets," *IEEE Trans. Antennas Propag.*, vol. 62, no. 8, pp. 4209–4219, Aug. 2014.

[6] Q. Zhang, J. Hu, Y. Luo, and Y. J. Chen, "Research progresses in radar feature extraction, imaging, and recognition of target with micro-motions," *J. Radar*, vol. 7, no. 5, pp. 531–647, Oct. 2018.

[7] F. Wang, L. Zhang, Y. Cao, and G. Wang, "Integrating motion compensation with polar format interpolation for enhanced highly squinted airborne SAR imagery," *IEEE Access*, vol. 7, pp. 177101–177113, 2019.

[8] B. Tian, Z. Lu, Y. Liu, and X. Li, "High velocity motion compensation of IFDS data in ISAR imaging based on adaptive parameter adjustment of matched filter and entropy minimization," *IEEE Access*, vol. 6, pp. 34272–34278, 2018.

[9] V. Brancato, M. Jäger, R. Scheiber, and I. Hajnsek, "A motion compensation strategy for airborne repeat-pass SAR data," *IEEE Geosci. Remote Sens. Lett.*, vol. 15, no. 10, pp. 1580–1584, 2018.

[10] Y. Wang, C. Feng, Y. Zhang, and S. He, "Translational motion compensation of space micromotion targets using regression network," *IEEE Access*, vol. 7, pp. 155038–155047, 2019.

[11] W. Pu, Y. Huang, J. Wu, H. Yang, and J. Yang, "Fast compressive sensing-based SAR imaging integrated with motion compensation," *IEEE Access*, vol. 7, pp. 53284–53295, 2019.

[12] Q. Dong, M.-D. Xing, X.-G. Xia, S. Zhang, and G.-C. Sun, "Moving target refocusing algorithm in 2-D wavenumber domain after BP integral," *IEEE Geosci. Remote Sens. Lett.*, vol. 15, no. 1, pp. 127–131, Jan. 2018.

[13] J. Xu, J. Cai, Y. Sun, X.-G. Xia, A. Farina, and T. Long, "Efficient ISAR phase autofocus based on eigenvalue decomposition," *IEEE Geosci. Remote Sens. Lett.*, vol. 14, no. 12, pp. 2195–2199, Dec. 2017.

[14] C. Noviello, G. Fornaro, P. Braca, and M. Martorella, "Fast and accurate ISAR focusing based on a Doppler parameter estimation algorithm," *IEEE Geosci. Remote Sens. Lett.*, vol. 14, no. 3, pp. 349–353, Mar. 2017.

[15] D. Ligori, S. Wagner, L. Fabbrini, M. Greco, T. Bieker, G. Pinelli, and S. Brüggenwirth, "Nonparametric ISAR autofocusing via entropy-based Doppler centroid search," *IEEE Geosci. Remote Sens. Lett.*, vol. 15, no. 11, pp. 1725–1729, Nov. 2018.

[16] T. B. Pittman, Y. H. Shih, D. V. Strekalov, and A. V. Sergienko, "Optical imaging by means of two-photon quantum entanglement," *Phys. Rev. A, Gen. Phys.*, vol. 52, no. 5, pp. R3429–R3432, Nov. 1995.

[17] A. Gatti, E. Brambilla, M. Bache, and L. A. Lugiato, "Ghost imaging with thermal light: Comparing entanglement and classical correlation," *Phys. Rev. Lett.*, vol. 93, no. 9, Aug. 2004, Art. no. 093602.

[18] R. Meyers, K. S. Deacon, and Y. Shih, "Ghost-imaging experiment by measuring reflected photons," *Phys. Rev. A, Gen. Phys.*, vol. 77, no. 4, Apr. 2008, Art. no. 041801R.

[19] D. Duan, S. Du, and Y. Xia, "Multiwavelength ghost imaging," *Phys. Rev. A, Gen. Phys.*, vol. 88, no. 5, Nov. 2013.

[20] D. Li, X. Li, Y. Qin, Y. Cheng, and H. Wang, "Radar coincidence imaging: An instantaneous imaging technique with stochastic signals," *IEEE Trans. Geosci. Remote Sens.*, vol. 52, no. 4, pp. 2261–2277, Apr. 2014.

[21] X. Zhou, H. Wang, Y. Cheng, and Y. Qin, "Radar coincidence imaging by exploiting the continuity of extended target," *IET Radar, Sonar Navigat.*, vol. 11, no. 1, pp. 60–69, Jan. 2017.

[22] X. Zhou, H. Wang, Y. Cheng, and Y. Qin, "Sparse auto-calibration for radar coincidence imaging with gain-phase errors," *Sensors*, vol. 15, no. 11, pp. 27611–27624, Oct. 2015.

[23] Y. Guo, X. He, and D. Wang, "A novel super-resolution imaging method based on stochastic radiation radar array," *Meas. Sci. Technol.*, vol. 24, no. 7, Jul. 2013, Art. no. 074013.

[24] X. Zhou, H. Wang, Y. Cheng, and Y. Qin, "Radar coincidence imaging with phase error using Bayesian hierarchical prior modeling," *J. Electron. Imag.*, vol. 25, no. 1, Jan. 2016, Art. no. 013018.

[25] S. Zhu, A. Zhang, Z. Xu, and X. Dong, "Radar coincidence imaging with random microwave source," *IEEE Antennas Wireless Propag. Lett.*, vol. 14, pp. 1239–1242, 2015.

[26] S. Zhu, Y. He, H. Shi, A. Zhang, Z. Xu, and X. Dong, "Mixed mode radar coincidence imaging with hybrid excitation radar array," *IEEE Trans. Aerosp. Electron. Syst.*, vol. 54, no. 4, pp. 1589–1602, Aug. 2018.

[27] S. Zhu, X. Dong, M. Zhang, R. Lu, J. Li, X. Chen, and A. Zhang, "A super-resolution computational coincidence imaging method based on SIMO radar system," *IEEE Geosci. Remote Sens. Lett.*, vol. 14, no. 12, pp. 2265–2269, Dec. 2017.

[28] G. Zha, H. Wang, Z. Yang, Y. Cheng, and Y. Qin, "Angular resolution limits for coincidence imaging radar based on correlation theory," in *Proc. IEEE Int. Conf. Signal Process., Commun. Comput. (ICSPCC)*, Sep. 2015, pp. 1–4.

[29] C. Zhao, W. Gong, M. Chen, E. Li, H. Wang, W. Xu, and S. Han, "Ghost imaging LiDAR via sparsity constraints," *Appl. Phys. Lett.*, vol. 101, no. 14, Oct. 2012, Art. no. 141123.

[30] S. Park, E. Kim, C.-H. Sohn, and J. Park, "Dynamic contrast-enhanced MR angiography exploiting subspace projection for robust angiogram separation," *IEEE Trans. Med. Imag.*, vol. 36, no. 2, pp. 584–595, Feb. 2017.

[31] Y. Cheng, Z. Zhou, X. Xu, Y. Qin, and H. Wang, "Radar coincidence imaging with stochastic frequency modulated array," *IEEE J. Sel. Topics Signal Process.*, vol. 11, no. 2, pp. 414–422, Mar. 2017.

[32] Z. Yang, L. Xie, and C. Zhang, "Off-grid direction of arrival estimation using sparse Bayesian inference," *IEEE Trans. Signal Process.*, vol. 61, no. 1, pp. 38–43, Jan. 2013.

[33] E. J. Candès, M. B. Wakin, and M. B. Wakin, "An introduction to compressive sampling," *IEEE Signal Process. Mag.*, vol. 25, no. 2, pp. 21–30, Mar. 2008.

[34] A. V. Diebold, M. F. Imani, T. Sleasman, and D. R. Smith, "Phaseless computational ghost imaging at microwave frequencies using a dynamic metasurface aperture," *Appl. Opt.*, vol. 57, no. 9, pp. 2142–2149, Mar. 2018.
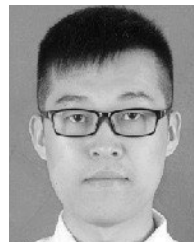
RUI LI was born in Heilongjiang, China, in 1992. He received the M.S. degree in electronic science and technology from the Institute of Equipment Management and Safety Engineering, Air Force Engineering University (AFEU), Xi'an, China, in 2016. He is currently pursuing the Ph.D. degree in electrical engineering with the Institute of Information and Navigation, AFEU. His current research interests include signal processing and radar imaging.

YING LUO (Member, IEEE) was born in Hunan, China, in 1984. He received the M.S. degree in electrical engineering from the Institute of Telecommunication Engineering, Air Force Engineering University (AFEU), Xi'an, China, in 2008, and the Ph.D. degree in electrical engineering from AFEU, in 2013. He was a Postdoctoral Fellow with the National Laboratory of Radar Signal Processing and a Xidian Scholar with the Department of Electrical and Computer Engineering, National University of Singapore, Singapore, from 2017 to 2018. He is currently an Associate Professor/Ph.D. Advisor with the Institute of Information and Navigation, AFEU. He is also an Adjunct Associate Professor with the Key Laboratory for Information Science of Electromagnetic Waves, Ministry of Education, Fudan University. He has published two books and over 80 papers on journals and conferences. Two of these articles won the First-Grade Prize of Shaanxi Natural Science Excellent Academic Paper in 2010 and 2013. His research interests include signal processing and auto target recognition (ATR) in SAR and ISAR.

QUN ZHANG (Senior Member, IEEE) received the M.S. degree in mathematics from Shaanxi Normal University, Xi'an, China, in 1988, and the Ph.D. degree in electrical engineering from Xidian University, Xi'an, in 2001. He was a Research Engineer and a Research Fellow with the Department of Electrical and Computer Engineering, National University of Singapore, Singapore, from 2001 to 2003 and 2005 to 2006, respectively. He has published over 200 papers on journals and conferences. His main research interests include signal processing, clutter suppression, and its application in SAR and ISAR.
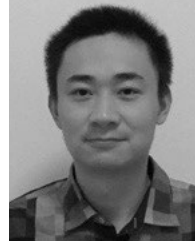
DAN WANG was born in Anhui, China, in 1990. He received the M.S. degree in information and communication engineering from the College of Electronic Science and Engineering, National University of Defense Technology, Changsha, China, in 2013. He is currently pursuing the Ph.D. degree in electrical engineering with the Institute of Information and Navigation, Air Force Engineering University (AFEU), Xi'an, China. He is currently with the Radar and Signal Processing Laboratory, Institute of Information and Navigation, AFEU, and also with the Collaborative Innovation Center of Information Sensing and Understanding. His current research interests include signal processing and radar imaging.

● ● ●
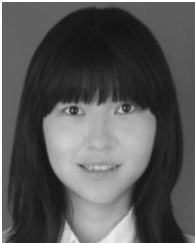
YI-JUN CHEN was born in Shaanxi, China, in 1989. She received the M.S. and Ph.D. degrees in electrical engineering from the Institute of Information and Navigation, Air Force Engineering University (AFEU), Xi'an, China, in 2013 and 2017, respectively.

She is currently working with the College of Information Engineering, Engineering University of PAP, Xi'an. Her current research interests include signal processing and cognitive radar.